

# π-Conjugated Metal Free Porphyrin as Organic Cathode for Aluminum Batteries

Shagor Chowdhury,<sup>\*[a, b]</sup> Noha Sabi,<sup>[c, d]</sup> Rafael Córdoba Rojano,<sup>[c]</sup> Nolwenn Le Breton,<sup>[e]</sup> Athanassios K. Boudalis,<sup>[e]</sup> Svetlana Klayatskaya,<sup>\*[a]</sup> Sonia Dsoke,<sup>\*[c, f, g]</sup> and Mario Ruben<sup>\*[a, b, h]</sup>

Nowadays, Al (dual) batteries are mainly based on graphite cathode materials. Besides this material, the limited life cycle and the rate performance of other possible cathode materials have hampered the development of practical and sustainable rechargeable aluminium batteries (RABs). Herein, we report an organic A<sub>4</sub>-metal-free porphyrin system bearing diphenylami-

mo-phenyl functional units as an Al-storage cathode material, which is capable of delivering a reversible capacity of 83 mAhg<sup>-1</sup> at 1 Ag<sup>-1</sup> after 200 cycles and displays a good cycling stability. Achieving such high rate performance opens a pathway to developing practical sustainable cathodes for aluminium batteries.

## Introduction

Nowadays, there is a significant and fast-growing demand for portable electronic devices and electric vehicles, most of which rely on lithium-ion batteries (LIBs). This technological shift has revolutionized our society. The manufacturing of LIBs requires various input materials, including lithium, nickel, and cobalt, mainly extracted from ores with limited resources. Graphite is another of the critical components used in LIBs, but it is produced in specific regions worldwide. Consequently, geopolitical concerns about the limited supply of these resources and the associated negative environmental impact have intensified as our reliance on these resources continues to rise.<sup>[1]</sup> Therefore, it is crucial to find and harness sustainable energy storage systems that can replace or complement LIBs.<sup>[2]</sup>

In this prospect, Aluminum metal offers great potential over other metals due to its abundance (8.1 wt% in the Earth's crust), high theoretical volumetric capacity (8,056 mAh cm<sup>-3</sup>), safety, and low cost. Moreover, aluminum is not rated as critical in the reserves-to-production ratio, political, and supply risks because it originates from various sources, and its recyclability methods are well-established.<sup>[3]</sup> Despite these positive features, developing efficient electrode materials with which aluminum ions can reversibly interact is still a bottleneck. The development of suitable cathode materials is mainly hindered by their limited stability in the corrosive aluminum-based electrolytes based on an ionic liquid salt mixed with AlCl<sub>3</sub><sup>[4]</sup> and by the low discharge voltage and capacity decay. According to the different energy storage mechanisms, the cathode materials (investigated so far) can be categorized as intercalation-types and conversion types.<sup>[5]</sup> In 2015, Dai's group reported a novel secondary aluminum battery with high-rate capability, attracting attention from the battery community.<sup>[6]</sup> The cell consisted of a three-dimensional graphitic-foam as the positive electrode and an aluminum foil as the negative one and could deliver a specific capacity of 70 mAhg<sup>-1</sup>. Following this work, several inorganic positive electrode materials have been developed, including transition metal oxides,<sup>[7]</sup> sulfides,<sup>[8]</sup> selenides,<sup>[9]</sup> and sulfur.<sup>[10]</sup> However, these materials suffer from low capacity,

- [a] S. Chowdhury, S. Klayatskaya, M. Ruben  
Institute of Nanotechnology (INT), Karlsruhe Institute of Technology (KIT)  
Eggstein-Leopoldshafen 76344, Germany  
E-mail: schowdhury@unistra.fr  
svetlana.klayatskaya@kit.edu  
mario.ruben@kit.edu
- [b] S. Chowdhury, M. Ruben  
Centre Européen de Sciences Quantiques (CESQ), Institut de Science et d'Ingénierie Suparamolaïculaires (ISIS)  
Strasbourg Cedex 67083, France
- [c] N. Sabi, R. C. Rojano, S. Dsoke  
Institute for Applied Materials (IAM), Karlsruhe Institute of Technology (KIT)  
Hermann-von-Helmholtz-Platz 1  
76344 Eggstein-Leopoldshafen, Germany
- [d] N. Sabi  
High Throughput Multidisciplinary Research (HTMR), Mohammad VI Polytechnic University  
Lot 660 Hay Moulay Rashid  
Ben Guerir, 43150, Morocco
- [e] N. Le Breton, A. K. Boudalis  
Institut de Chimie de Strasbourg (UMR 7177, CNRS-Unistra), Université de Strasbourg  
Strasbourg 67081, France
- [f] S. Dsoke  
Albert-Ludwigs-University Freiburg,  
Department of Sustainable Systems Engineering (INATECH)  
Emmy-Noether-Straße 2  
79110, Freiburg, Germany
- [g] S. Dsoke  
Fraunhofer Institute for Solar Energy Systems,  
Dep. Electrical Energy Storage  
Heidenhofstr. 2  
79110 Freiburg, Germany
- [h] M. Ruben  
Institute for Quantum Materials and Technology (IQMT), Karlsruhe Institute of Technology (KIT)  
Eggstein Leopoldshafen 76344, Germany
-  Supporting information for this article is available on the WWW under <https://doi.org/10.1002/batt.202300285>
-  © 2024 The Authors. *Batteries & Supercaps* published by Wiley-VCH GmbH. This is an open access article under the terms of the Creative Commons Attribution License, which permits use, distribution and reproduction in any medium, provided the original work is properly cited.

rapid capacity fading, and low diffusion coefficient due to the strong electrostatic interactions between  $\text{Al}^{3+}$  ions and the positive electrode, and today still, graphite is the standard cathode used in Aluminum-based batteries (more specifically, Aluminum dual batteries).

In contrast, organic materials offer advantages such as lightweight, easy design, and flexible structure that can alleviate the induced strain upon electrochemical cycling. Moreover, the unique coordination chemistry of each organic material could avoid the steric repulsions induced by the intercalation of multivalent cations. In addition, organic cathode materials are based on abundant and lightweight elements such as C, O, and N (often related to oxygen or nitrogen-containing active sites in the form of carbonyl ( $\text{C}=\text{O}$ ) or imine ( $\text{C}=\text{N}$ ) functionality), and their activity is mainly based on coordination chemical reactions rather than intercalation.<sup>[11]</sup> Some recent works showcase organic cathode material for rechargeable aluminum batteries (RABs). Kim et al. have investigated a triangular phenanthrene-quinone-based macrocycle that exhibits a reversible capacity of  $110 \text{ mAh g}^{-1}$  with a cyclability over 5000 cycles<sup>[12]</sup> in another recent study, Han et al. compared the performances of  $\text{H}_2\text{TPP}$  and  $\text{H}_2\text{TCPP}$  in aluminum batteries. They report that  $\text{H}_2\text{TPP}$ , with a specific capacity of  $101 \text{ mAh g}^{-1}$  at  $100 \text{ mA g}^{-1}$ , performs better than  $\text{H}_2\text{TCPP}$ .<sup>[13]</sup> The redox properties of porphyrins result from the facile reduction and oxidation of the macrocyclic ring, and it has been demonstrated that the lone pair of electrons in the N atom functions as an active site, reacting with the aluminum cation.<sup>[13]</sup> However, the influence of the acidic electrolyte on the chemical properties of the porphyrins has not been evaluated yet, where the tetrapyrrole skeletons tend to gain two protons in an acidic environment to form a dication.<sup>[14]</sup>

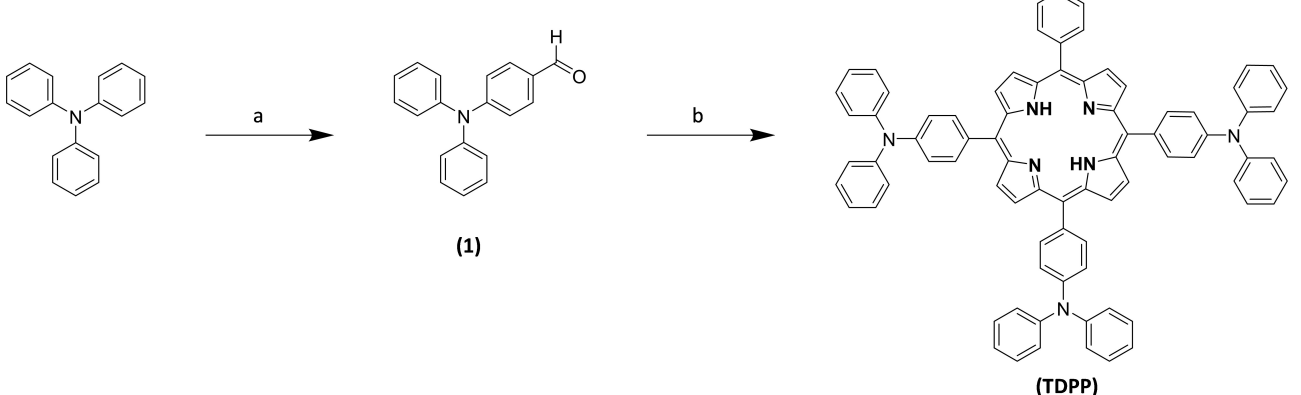
As our group has a longstanding interest in the development of porphyrin-based electrode materials,<sup>[15]</sup> we envisioned that porphyrins substituted with diphenyl amino-phenyl (TDPP) could serve as promising (RAB)-active material. This system has been chosen in particular because of: i) the bipolar nature of

porphyrin material that can either donate or accept electrons at its mesomeric core.<sup>[15c]</sup> ii) porphyrins generally have small HOMO-LUMO gaps that enable the facile uptake and release of electrons, thus, leading to fast redox kinetics,<sup>[16]</sup> iii) the diphenyl amino-phenyl functionality can store reversibly anionic aluminum complexes.<sup>[17]</sup> Moreover, TDPP is obtained by a straightforward method with a good yield, opposite to most of the prior studied systems, in which a multi-step synthesis is required, increasing their cost and resulting in poor yields. This porphyrin-based system further provides the opportunity to improve their performance through molecular engineering.<sup>[18]</sup> This can involve the introduction of metals or the alteration of their substituents to enhance both conductivity and stability.

## Results and Discussion

### Material Syntheses and Characterization

Scheme 1 shows the multi-step synthesis of (TDPP) 5,10,15,20-tetrakis[4-(diphenylamino)phenyl] porphyrin. This synthesis is based on a previously reported procedure [22] with improvements.<sup>[19]</sup> The starting point is the preparation of the precursor 4-(N,N-diphenylamino)-benzaldehyde (1) from triphenylamine (Vilsmeier-Haack reaction), then a standard Rothemund condensation reaction is performed between the pyrrole and (1) in a propionic acid, yielding the corresponding TDPP in 40% yield. The structure has been confirmed by  $^1\text{H}$  NMR spectroscopy, associated COSY map (see Figures S1 and S2),  $^{13}\text{C}$  NMR spectroscopy (see Figure S4), mass spectroscopy (see Figure S6 and S7), and UV-vis spectroscopy (see Figure S8). The material is semi-crystalline, as revealed by powder XRD (see Figure S9).



**Scheme 1.** Schematic representation of the chemical synthesis of TDPP. a)  $\text{POCl}_3$ , DMF,  $80^\circ\text{C}$ , 1 h, 90 %. b) Propionic acid, pyrrole,  $142^\circ\text{C}$ , 4 h, 40 %.

## Electrochemical characterization

Electrochemical measurements have been performed using two electrodes, Swagelok-type cells with tungsten rods in which the TDPP was utilized as the positive electrode and aluminum as both reference and counter electrode. The ionic liquid 1-ethyl-3-methylimidazolium (EMIm) chloride with 1.5 added equivalents of AlCl<sub>3</sub> (AlCl<sub>3</sub>:[EMIm]Cl = 1.5:1) served as the electrolyte due to its wide electrochemical window, good ionic conductivity, and relatively low viscosity.<sup>[20]</sup>

Figure 1 shows the cyclic voltammetry of the TDPP-based electrodes versus Al metal. During the first cycle, six anodic peaks appear at 1.05, 1.21, 1.45, 1.86, 2.0, and 2.19 V, respectively. While in the cathodic scan, three prominent cathodic peaks are visible at 2.07, 1.76, and 1.35 V. On repeated cycling, significant changes take place between the first and the fifth CV cycle, in which the anodic peaks located at 1.86 and 2.0 V merge into one peak located at 1.82 V, while the peaks located at 1.05 and 1.21 V disappear after the first cycle and resulted in three reversible redox peaks ( $E^{(1/2)} = 1.36$  V,  $E^{(1/2)} = 1.76$  V, and  $E^{(1/2)} = 2.12$  V). Further cycling (20<sup>th</sup> to 120<sup>th</sup> cycles) results in anodic peaks (as previously observed) at 1.81 and 2.19 V, two broad cathodic peaks at 1.746 and 1.31 V, and an irreversible cathodic peak at 0.78 V. These peaks could originate from the redox reaction of [TDPP] implemented by donating  $\pi$  electrons (from  $18\pi$  to  $16\pi$ ) and to the formation of N(radical) cations ( $R_3N^{+}\bullet$ ) in – (diphenylamino) – phenyl substituents (Figure S10).<sup>[17,21]</sup> On the other hand, the peaks located at 1.05 and 1.21 V, visible only in the first cycle, could be explained by a possible cathode electrolyte interface (CEI) formation and some irreversible chemical reactions between the electrode and electrolyte (this last point will be discussed in the following sections). Therefore, we hypothesize that TDPP undergoes structural modification upon cycling, and to differentiate the sample from the initial TDPP, the material will be denoted as

[TDPP]. It is worth mentioning that the current contribution of carbon black coated on carbon paper is negligible (Figure S11). With increasing cycles, both anodic and cathodic peak intensities increase and become sharper, which might be attributed to an activation process and improved utilization of the active sites.<sup>[22]</sup>

The charge/discharge profile of TDPP at 100 and 1000 mA g<sup>-1</sup> are presented in Figure 2. The electrode was initially cycled five times at 100 mA g<sup>-1</sup> and then cycled at 1000 mA g<sup>-1</sup>. Herein, [TDPP] delivers an initial charge/discharge capacity of 830/132 mAh g<sup>-1</sup> at 0.1 A g<sup>-1</sup>. Irreversible charge/discharge capacities are frequently observed in porphyrin-based electrodes, it is attributed to the formation of solid electrolyte interphase and due to side reactions because of the initial incorporation of the anions.<sup>[15a,d, 18, 23]</sup> A stable discharge capacity is around 125 mAh g<sup>-1</sup> after the first cycle at a current density of 100 mA g<sup>-1</sup> (2<sup>nd</sup> to 5<sup>th</sup> cycle) was recorded, equal to the theoretical capacity calculated for six e<sup>-</sup> processes. Increasing the current density to 1 A g<sup>-1</sup> resulted in a drastic decrease in the capacity values that stabilizes around 84 mAh g<sup>-1</sup> at the 10th cycle. Furthermore, the presence of plateaus during the initial early stage of cycling suggests the presence of a multi-electron transfer mechanism and similar reaction pathways throughout the cycling. This stability of the material was evaluated by electrochemical impedance spectroscopy recorded after the 10<sup>th</sup> and 50<sup>th</sup> cycles (Figure S12). The spectra recorded during the charging or discharging processes after the 10<sup>th</sup> and the 50<sup>th</sup> cycles are similar, suggesting good stability and electrode integrity. After 200 cycles, the material can still deliver a specific discharge capacity of 83 mAh g<sup>-1</sup> with a high-capacity retention, illustrating superior reversibility in ion shuttling.

The long-term cycling performance of [TDPP] was also investigated at 1000 mA g<sup>-1</sup> and the values of the first 50 cycles are presented in Figure 3(a), while Figure 3(b) displays the

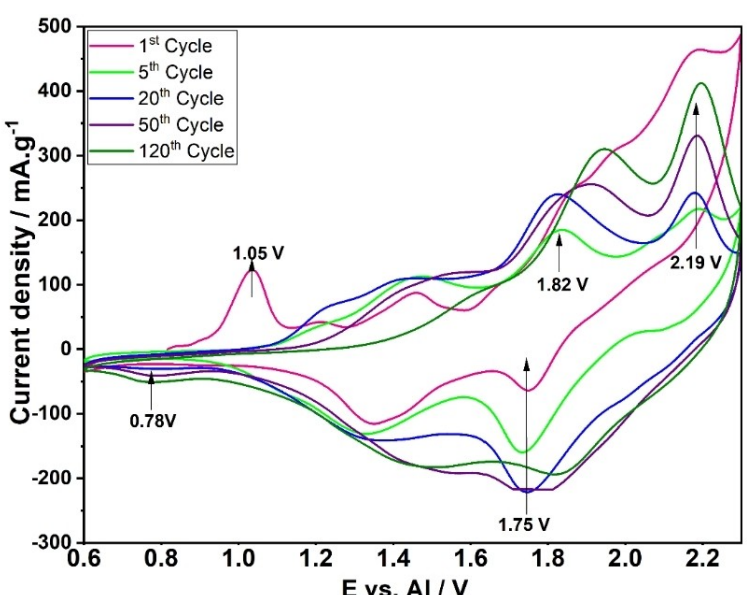


Figure 1. (a) Cyclic voltammetry of TDPP recorded between 0.6–2.3 V vs. Al at scan rate 0.5 mVs<sup>-1</sup>.

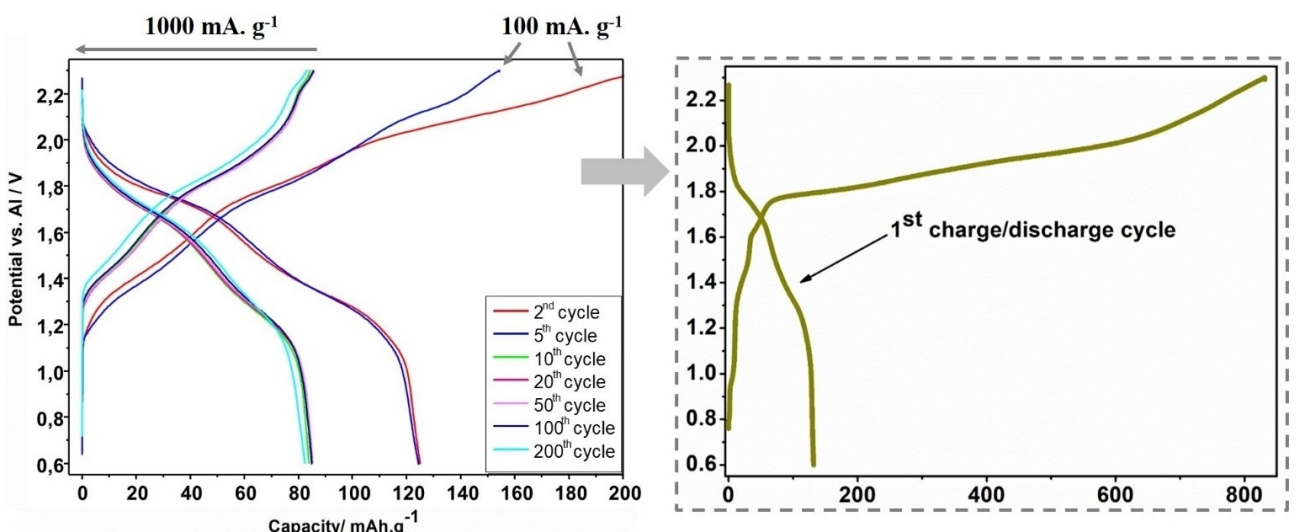


Figure 2. Charge/discharge curves of TDPP at 100 and  $1000 \text{ mA g}^{-1}$  in the potential window 0.6–2.3 V vs. Al.

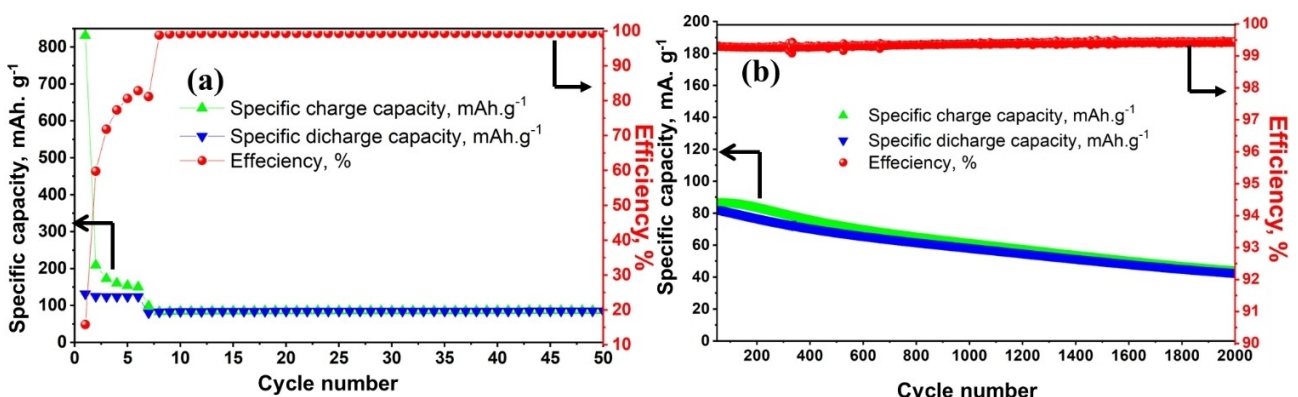


Figure 3. Cyclic performance of TDPP at  $1 \text{ Ag}^{-1}$  a) 50 cycles in which the initial five cycles were performed at  $0.1 \text{ Ag}^{-1}$  b) 2000 cycles.

capacity extended to 2000 cycles. The cell was initially cycled five times at  $100 \text{ mA g}^{-1}$  and then at  $1000 \text{ mA g}^{-1}$ . The capacity decreases during the first seven cycles until it stabilizes at  $85 \text{ mA h g}^{-1}$  in the 15<sup>th</sup> cycle. The initial coulombic efficiency is 16% and then increases over cycling, reaching 99% at the 10<sup>th</sup> cycle (Figure 3(a)). The capacity retention (calculated based on the 10<sup>th</sup> cycle) is relatively high, reaching 97% after 200 cycles and 85% after 500 cycles. Following that, significant fading in capacity was observed, with a retention of 51% after the 2000 cycles. Nevertheless, these findings obtained on a laboratory scale under non-optimized conditions indicate the material's high potential as a positive electrode with good cycling stability for 500 cycles in an aggressive electrolyte.

Rate capability was carried out to evaluate the feasibility of this battery cell for high-power applications (Figure 4). At the lowest applied current of  $40 \text{ mA g}^{-1}$ , [TDPP] displays initial charge and discharge capacities of 592 and  $85 \text{ mA h g}^{-1}$ , and in the following cycles, the charge capacity drops to  $136 \text{ mA h g}^{-1}$ . Increasing the current density induces a drop in the charged capacity with improved efficiency. Precisely, at the current density of 50, 80, 100, 200, 300, 400, 600 and  $800 \text{ mA g}^{-1}$ ,

charge capacities (efficiency) of  $93 \text{ mA h g}^{-1}$  (84%),  $85 \text{ mA h g}^{-1}$  (88%),  $79 \text{ mA h g}^{-1}$  (92%),  $73 \text{ mA h g}^{-1}$  (97%),  $57 \text{ mA h g}^{-1}$  (97%),  $52 \text{ mA h g}^{-1}$  (98%),  $43 \text{ mA h g}^{-1}$  (98%) and  $42 \text{ mA h g}^{-1}$  (99%) are obtained, respectively (Figure S13). Its excellent rate performances and impressive cycling stability up to 2000 cycles (capacity retention of 51% at  $1000 \text{ mA g}^{-1}$ ) make this electrode material very promising for high-power devices (microelectronic systems: Pulse Power Applications, Electric Fences and Photo-flash Capacitors) that require short bursts of intense power rather than long-term energy supply.<sup>[24]</sup>

To understand the ion storage process in the [TDPP], CV tests were performed at various scan rates ranging from 0.1 to  $1.0 \text{ mV s}^{-1}$  (Figure 5 (a)). Following the method proposed by Dunn and coworkers<sup>[25]</sup> and using the equation  $i = av^b$ , the analysis allowed the calculation of the b-value from the slope of the  $\log(i)$  versus  $\log(v)$  plot. A b-value close to 1 indicates a surface-controlled process, while a value close to 0.5 indicates a diffusion-controlled one. The obtained b values from six sets of peaks are 0.99, 0.82, 0.74, 0.94, 1.03, and 1.29 (Figure 5(b)), indicating that the surface-controlled process mainly dominates the [TDPP] electrodes reaction with no or minor diffusion

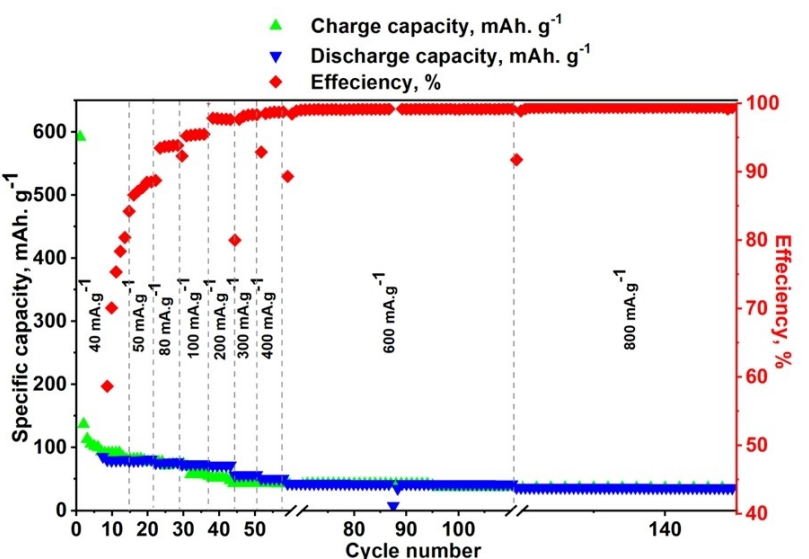


Figure 4. Rate capability of TDPP at different current densities of 40, 50, 80, 100, 200, 300, 400, 600 and 800 mA g<sup>-1</sup>.

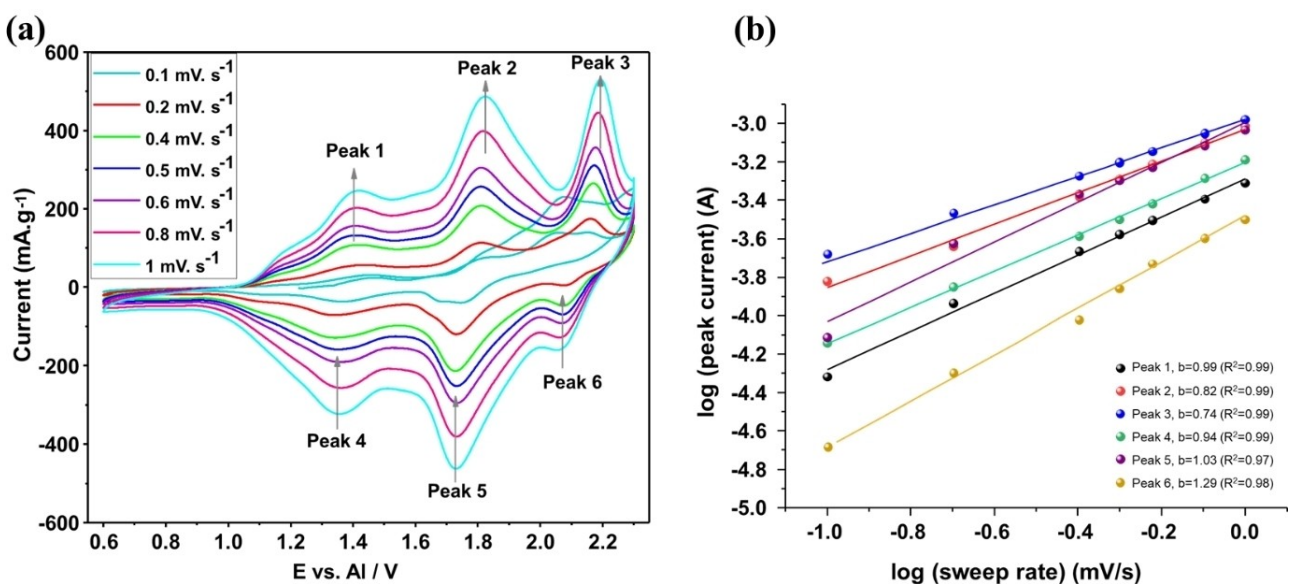


Figure 5. (a) CV curves of TDPP at various scan rates, (b)  $\log(i)$  versus  $\log(v)$ .

limitations. The surface-controlled contribution was then calculated to be 92% at a scan rate of  $0.5\text{ mV s}^{-1}$ , and the “surface-controlled process” contribution ratio kept increasing with increasing the scan rate (Figure S14).

#### Post-Mortem characterizations of TDPP

Postmortem analysis has been carried out to gain more insight into the structural modification in TDPP upon cycling. The cycled electrodes showed lower solubility in common organic solvents than the pristine ones (Figure S15), impeding their analyses by some characterization techniques like NMR. On the other hand, the change of solubility indicates the occurrence of

chemical modification of the material induced by the electrochemical reactions, evidenced by the morphological changes recorded by ex-situ SEM of TDPP in the pristine state and at different stages of cycling (Figure 6(a-d)). In the pristine state (Figure 6(a)), small irregular moss-like shaped particles with a porous structure are observed. After 105 cycles (Figure 6(b)), the surface appears smoother and denser, and the voids between the particles disappear along with the formation of agglomerates of different heights. After the 175<sup>th</sup> cycle (Figure 6(c)), the characteristic particle shape is no longer visible, but an interconnected surface is observed. The fibers observed in the SEM picture represent the remaining separator (glass fiber), which remains attached to the electrode. After 350 cycles (Figure 6(d)), the interconnected surface structure seems more

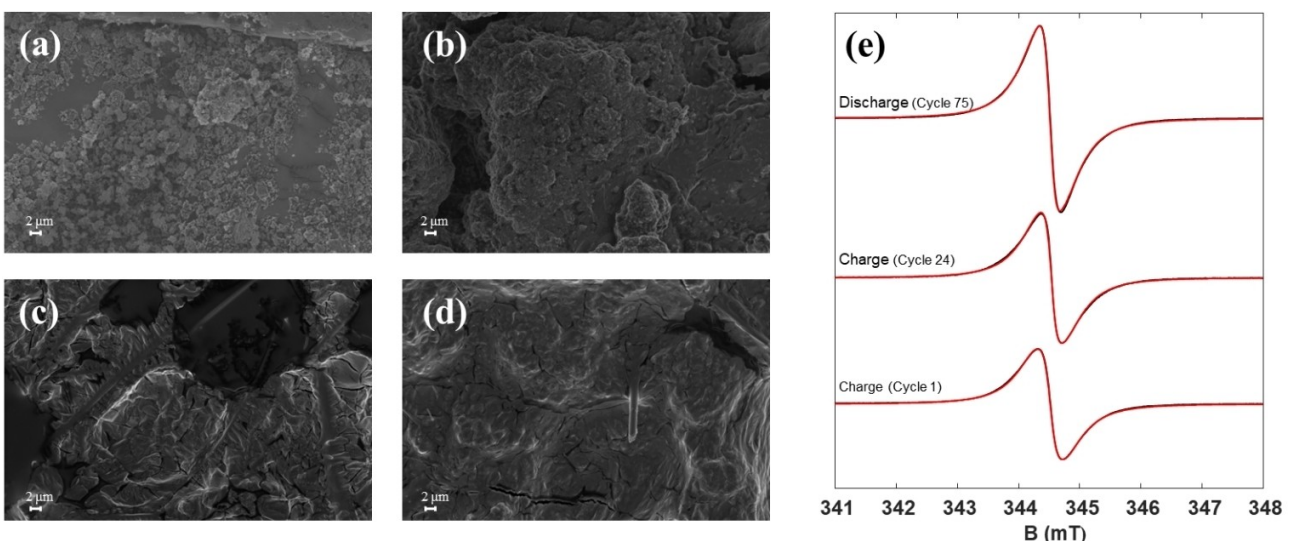


**Figure 6.** SEM images of the cycled TDPP electrode: (a) pristine state, after (b) 105 cycles, (c) 175 cycles, and (d) 350 cycles. (e) Experimental (black) and simulated (red) EPR spectra of the cycled TDPP at different stages: bottom (charged – cycle 1), middle (charged - cycle 24), and top (discharged – cycle 75).

developed over the electrode surface, suggesting the formation of larger-sized particles that might be a result of continuous polymerization of [TDPP] upon electrochemical cycling.

The ability of the diphenyl amino-phenyl moiety to electro-polymerize has been previously demonstrated by several authors (Figure S16), and this strategy has been used to inhibit their dissolution into the electrolyte.<sup>[17,26]</sup> This phenomenon can be revealed by Electron Paramagnetic Resonance (EPR) and Infra-red (IR) spectroscopy.

The EPR recorded at room temperature on cycled electrodes at different stages: cycle 1 (charged at 2.3 V vs. Al), cycle 24 (charged at 1.85 V vs. Al) and cycle 75 (discharged at 1.2 V vs. Al) (Figure 6e) revealed the presence of a stable organic radical with a signal centered at a g value of 2.0031. These spectra were simulated using Easyspin.<sup>[27]</sup> Several models were tested to fit the spectra to a unique species, considering different line broadenings (Gaussian, Lorentzian, or both). These, however, did not produce satisfactory results. Satisfactory fits were only obtained when spectra were fitted to two species. Best fits were obtained for one species with a Lorentzian peak-to-peak linewidth of 0.21 mT and another with a Lorentzian linewidth of 0.54 mT. The proportions used for the simulation are summarized in Table S1 (see supplementary data). The differences in proportions might be either due to the distribution of the radicals within different magnetic environments or due to the presence of the radicals within polymeric species of various sizes. Another key finding is the decrease in the line width of the recorded signal, suggesting a structural modification and the formation of the radical in an extended π-system that might have resulted from the oligomerization of the diphenyl amino-phenyl moiety in TDPP.<sup>[17,28]</sup>

The formation of the oligomer has been checked further by the ex-situ IR spectra recorded at different states of charge (Figure 7). In the fingerprint region, the two peaks at  $693\text{ cm}^{-1}$  and  $754\text{ cm}^{-1}$  correspond to the out-of-plane C–H bending

vibration of the peripheral phenyl group of diphenyl amino-phenyl moiety (Figure 7 – green spectrum). After cycling, the intensity of these peaks decreases, and a new peak at  $831\text{ cm}^{-1}$  has evolved, which is attributed to the C–C stretching vibration of the biphenyl group of the formed oligomer.<sup>[29]</sup> Further insights into the IR spectra revealed the absence of the absorption peak at  $1167\text{ cm}^{-1}$  corresponding to C–N vibrations during charging, and reappearance upon discharging process. The peak corresponding to asymmetric vibration of C=N ( $\nu = 1481\text{ cm}^{-1}$  porphyrin ring) shifts to  $1469\text{ cm}^{-1}$ . While the peak corresponding to ring stretching of C=N ( $\nu = 1592\text{ cm}^{-1}$ ), it more visible during discharge state compared to the charged state. These results suggest that the nitrogen atoms of both the porphyrin macrocycle and the (diphenylamino)-phenyl units might be the possible interaction sites of the anionic aluminum complex during the electrochemical reaction.

Solid-state UV-visible spectroscopic analysis at different states of charge/discharge has been employed to further evaluate the structural changes in the porphyrin upon electrochemical cycling. For comparative reasons, we checked the spectrum of TDPP both in the liquid state ( $\text{CHCl}_3$ ) and in the solid state (Figure 8(a)). Identical spectra are obtained in both states. An intense Soret band is observed at 439 nm, followed by four Q-band characteristics for free-base porphyrins, attributed to vibronic transitions along the x and y axes.

After the first charge (red spectrum in Figure 8(b)), a hypsochromic effect on the soret band ( $439\text{ nm} \rightarrow 432\text{ nm}$ ), followed by a decrease of the number of Q bands into two centered at 566 and 613 nm is observed. Additionally, a broad band centered at 749 nm is present. However, after 24 cycles, the charged material (1.85 V vs. Al, green spectrum in Figure 8b) displays a spectrum similar to the discharged one after 75 cycles (blue spectrum in Figure 8b). These changes include splitting the soret band into two bands around 417 nm and 489 nm and a broad absorption band centered at 760 nm.

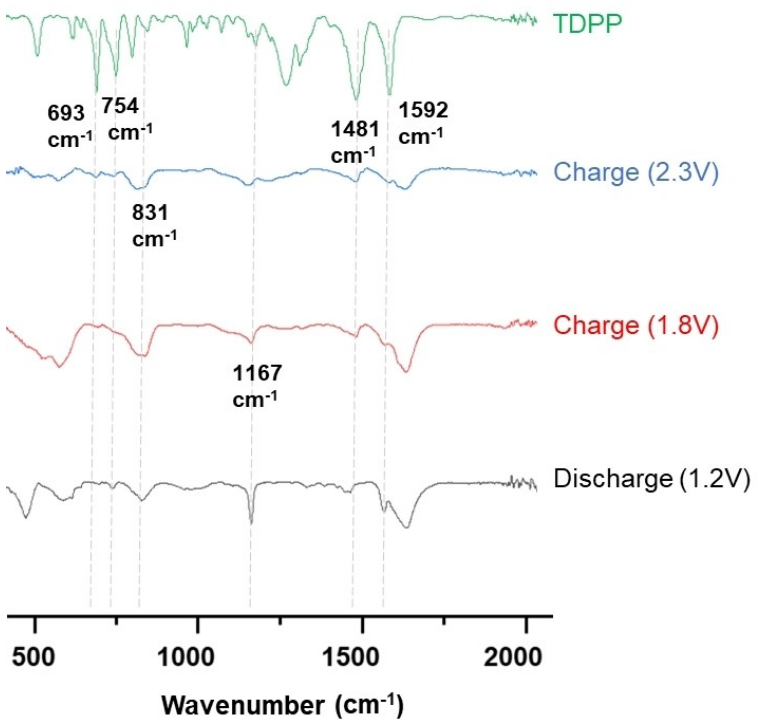


Figure 7. Ex-situ IR spectra of TDPP at different cycling: (green) TDPP, (blue) charged – cycle 1, (red) charged – cycle 24, and (black) discharged – cycle 75.

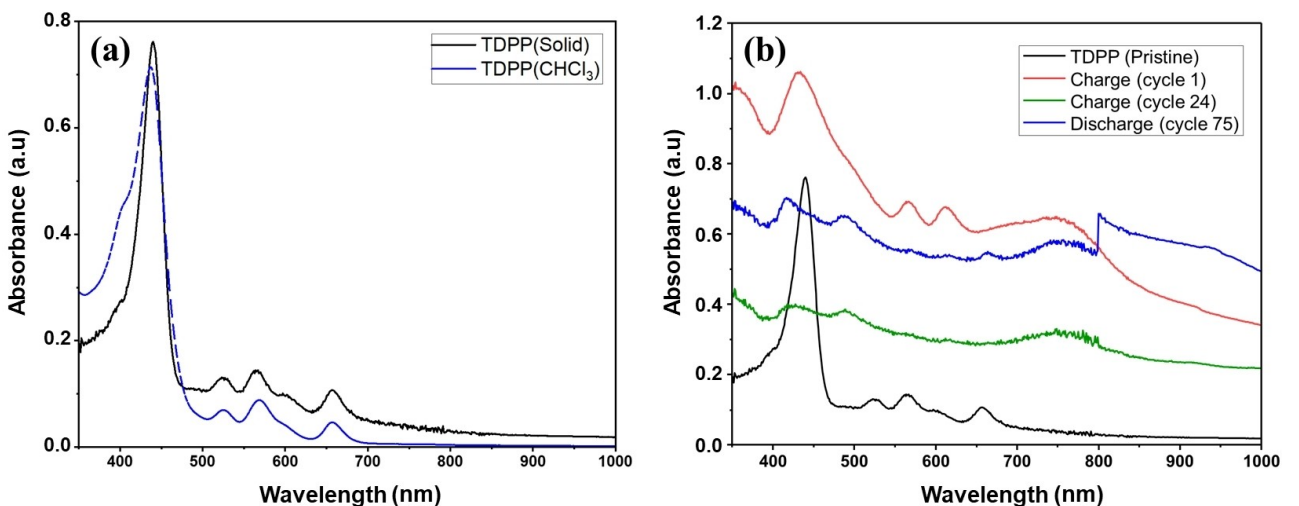


Figure 8. (a) UV-visible spectra of TDPP in solution and solid state; (b) UV-visible spectra of TDPP material in the pristine state, charged states (cycle 1), charged (cycle 24), and discharged (cycle 75).

Another key finding is the disappearance of the Q bands. This output indicates the formation of Hyperporphyrin during the cycling process, where the interior porphyrin nitrogens are protonated  $[(\text{TDPP}) \rightarrow (\text{TDPPH}_2)^{2+} \equiv [\text{TDPP}]]$  because of the acidity of the electrolyte ( $\text{pH} \approx 3$ ).

As a general statement, hyperporphyrins are defined as porphyrins that exhibit extra bands in the UV-visible when subjected to acidic or basic conditions. Characteristic fingerprints of hyperporphyrins are i) broadening and splitting of the Soret band and ii) red-shifted absorption beyond where the Q bands usually end.<sup>[30]</sup> Several literature studies show that

amino-substituted porphyrins exhibit a hyperporphyrin effect when subjected to acidic conditions.<sup>[31]</sup> To validate the proposed hypothesis, two UV-visible control experiments of TDPP were recorded: i) in the presence and absence of the electrolyte (Figure 9(a)) and ii) in the presence and absence of an organic acid Trifluoroacetic acid (TFA) (Figure 9(b)). The addition of the electrolyte or TFA results in similar spectra displaying identical absorption bands at 417 nm and 489 nm and a broad band centered at 769 nm, similar to those recorded for the cycled electrode (cycles 24 and 75). This hypothesis is further supported by <sup>1</sup>H-NMR analysis performed in the

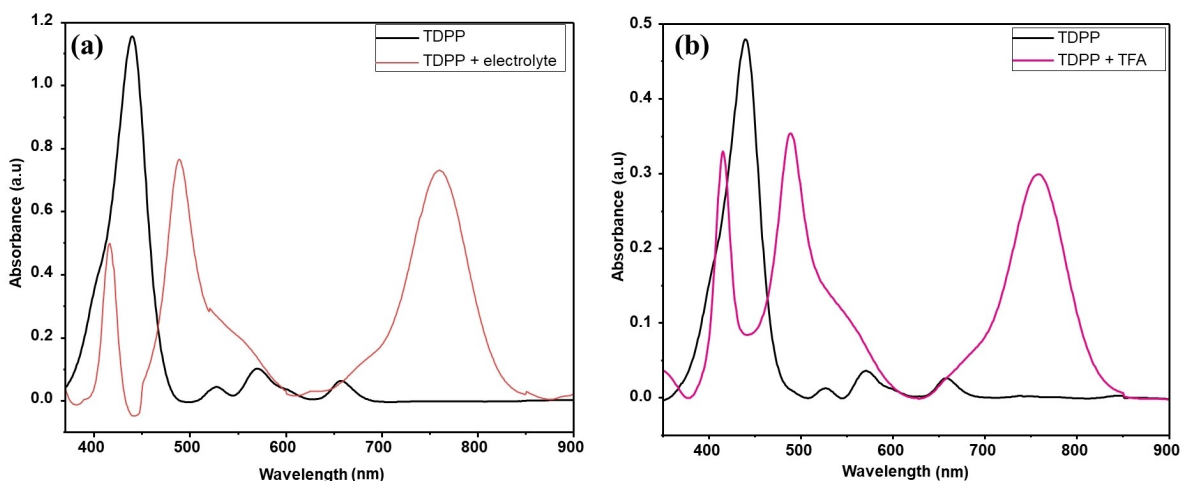


Figure 9. (a) UV-visible spectra of TDPP in the presence and absence of the electrolyte; (b) UV-visible spectra of TDPP in the presence and absence of TFA.

presence and absence of the electrolyte, confirming that the proton coordination environment involves the porphyrin ring (Figure S17).

All the experiments demonstrate that TDPP is converted into hyperporphyrin [TDPP] and reorganizes into an oligomeric structure upon cycling. The nature and the type of the oligomer are still undefined, and ongoing investigations are directed toward identifying and understanding the nature of the oligomer and its precise effect on the charge storage mechanism.

## Conclusions

In summary, TDPP porphyrin molecules have been proven to be functional as positive electrode materials for organic RABs. The material is able to deliver a reversible capacity of  $83 \text{ mAh g}^{-1}$  at  $1 \text{ A g}^{-1}$  with high-capacity retention (97 %) after 200 cycles, which stands for good cycling stability. Ex-situ IR, SEM, and EPR indicate the formation of oligomers upon cycling. Meanwhile, the UV-visible spectroscopic studies highlight the formation of hyperporphyrin. The nitrogen in the porphyrin ring and the (diphenylamino)-phenyl unit are most likely to act as the storage sites for the anionic aluminium complex, as revealed by IR spectroscopy. This work opens a new way for developing organic positive electrode materials for long-term and safe energy storage.

## Methods

All reagents were obtained commercially unless otherwise noted. All reactions were performed in oven-dried glassware under an argon atmosphere. All solvents were dried and distilled by standard procedures. Thin-layer chromatography was performed on aluminum plates pre-coated with Merck 5735 silica gel 60 F<sub>254</sub>. Column chromatography was performed with Merck silica gel 60 (230–400 mesh). <sup>1</sup>H NMR spectra were recorded on a Bruker DRX 400 spectrometer; chemical shifts are given in ppm using residual

proton resonances of the solvents as references. UV-VIS spectra were measured on a Varian Cary 500 Scan UV/VIS/NIR spectrophotometer and solid-state UV-Vis with an integrating sphere. Scanning electron microscope (SEM) images were collected using a ZEISS LEO 1530 instrument with an X-Max Silicon Drift Detector. Mass spectrometry measurements were carried out using ThermoFisher Ultimate3000 with Scientific Vanquish Flex UHPLC with electrospray ionization (ESI) and Maldi Autoflex speed Bruker. X-band EPR spectra were recorded on an ESP300E (Bruker Biospin GmbH) spectrometer equipped with a high sensitivity resonator (4119HSW, Bruker). Measurements were done with a modulation amplitude of 0.03 mT at a frequency of 100 kHz. The microwave frequency was 9.658 GHz with a power of 0.05 mW. Spin quantification was done by comparing the double integral of the EPR spectra to the double integral of a freshly homemade standard consisting of a 4.81 mg sample of a 1.8 % w/w mixture of DPPH in KCl.

## Synthesis of TDPP

**4-(N,N-Diphenylamino)-benzaldehyde (1):** In a 100 mL two-necked equipped with a water condenser, Phosphorus oxychloride (4 g, 026 mmol) was added to DMF (3.2 g, 42 mmol) slowly at 0 °C. After that, it was heated to 30 °C, followed by the rapid addition of Triphenylamine (2.55 g, 0.01 mmol). The mixture was heated to 50 °C, stirred for 2 h, and poured into ice. Sodium hydroxide was used to neutralize the solution to pH between 10 and 11, and then the suspension was heated to 80 °C and stirred for 1 h. The residue was filtered and purified by column chromatography using silica gel with CH<sub>2</sub>Cl<sub>2</sub> as the eluent to obtain the yellow solid (2.4 g, 90% yield). <sup>1</sup>H NMR (400 MHz, CDCl<sub>3</sub>) δ 9.81 (s, 1H), 7.68 (d, J = 8.7 Hz, 2H), 7.40–7.29 (m, 4H), 7.17 (m, 6H), 7.01 (d, J = 8.7 Hz, 2H). HR-MS (ESI<sup>+</sup>) calc. for: [M + H]<sup>+</sup> m/z = 274.1226, found m/z = 274.1222.

**(TDPP):** In a 100 mL two-necked round-bottomed flask equipped with a water condenser, a mixture of 4-(N,N-Diphenylamino)-benzaldehyde (1) (4 g, 14 mmol) and fresh pyrrole (1.01 mL, 14 mmol) in propionic acid (40 mL) were added under argon. The reaction solution was heated up to 140 °C for 4 h. After cooling to room temperature; the solution was evaporated under reduced pressure and then subjected to column chromatography on silica gel and dried under vacuum to obtain the desired product as a brown solid (1.8 g, 40% yield). <sup>1</sup>H NMR (400 MHz, CDCl<sub>3</sub>) δ 9.00 (s, 8H), 8.09 (d, J = 8.5 Hz, 8H), 7.46 (d, J = 8.5 Hz, 8H), 7.42 (d, J = 4.2 Hz, 32H), 7.15 (m, 8H), -2.67 (s, 2H). <sup>1</sup>H NMR (400 MHz, CDCl<sub>3</sub>): 121.38, 123.29, 124.87, 126.23, 129.19, 129.35, 129.52, 129.81,

135.67, 136.03, 147.86. MALDI-TOF (m/z): calcd for  $C_{92}H_{66}N_8$ , 1282.5410; found,  $[M + H]^+$  1283.8. HR-MS (ESI $^+$ ) calc. for:  $[M + H]^+$  m/z = 1283.5483, found m/z = 1283.5480.

### Electrodes preparation and electrochemical measurements

The positive electrode materials were prepared by mixing 60% of the active material, 30% of carbon black (to improve the electronic conductivity), and 10% of the polyacrylonitrile dissolved in DMSO. The resulting suspension was stirred overnight, spread on carbon paper (QUINTECH), and finally dried overnight under the fume hood at ambient conditions. The resulting coating was further dried in the oven for 4 h at 80 °C, and then 12 mm diameter electrodes were punched out. The electrodes were dried for 12 h in a vacuum oven under 110 °C. The active electrode materials have masses in the interval of 1.6–1.8 mg. Two electrodes of Swagelok-type cells with tungsten rods were used. As counter and reference electrodes, aluminum electrodes with 12 mm diameter, supplied from Goodfellow (with 99% purity and 0.1 mm thickness) were used. As the separator, two glass-fiber disks (Whatman GF/D) were used. The cells were galvanostatically charged and discharged with a VMP3 (Biologic) battery testing system at room temperature at different currents and in the potential window 0.6–2.3 V vs. Al. Cyclic voltammetry was done at 0.5 mVs $^{-1}$  scan rate. The capacity retention was calculated based on the 10<sup>th</sup> cycle, where the capacity stabilized. Multi-rate cyclic voltammetry was performed at different scan rates (0.1, 0.2, 0.4, 0.5, 0.6, 0.8 and 1 mVs $^{-1}$  to investigate the pseudo-capacitive behavior of the investigated compound in the potential window 0.6–2.3 V. Electrochemical impedance spectroscopy (EIS) test was performed on a VMP-3 (Bio-Logic) potentiostat at different state of charge and after 10 and 50 cycles in the frequency interval 0.1 MHz to 6 Hz with a voltage amplitude of 10 mV, in the potential window 0.6–2.3 V.

### Electrolyte preparation

The ionic liquid-based electrolyte was prepared and handled in an argon-filled glovebox (MBraun, O<sub>2</sub>, H<sub>2</sub>O < 0.5 ppm). The preparation consists of a slow addition of AlCl<sub>3</sub> (anhydrous, Sigma Aldrich, 99,99%) to EMImCl (Sigma-Aldrich, > = 95%) at a molar ratio of 1.5/1 (AlCl<sub>3</sub>/EMImCl). The mixture was stirred using a magnetic bar at room temperature.<sup>[32]</sup> The final solution is a yellowish viscous liquid.

### Acknowledgements

This work contributes to the research performed at CELEST (Center for Electrochemical Energy Storage Ulm-Karlsruhe) and was funded by the German Research Foundation (DFG) under Project ID 390874152 (POLiS Cluster of Excellence). SC wishes to thank the Foundation Jean-Marie Lehn project "QBIRAD" for the financial funding. Open Access funding enabled and organized by Projekt DEAL.

### Conflict of Interests

The authors declare no conflict of interest.

### Data Availability Statement

The data that support the findings of this study are openly available at <https://zenodo.org/records/10281805>.

**Keywords:** Non-aqueous aluminum batteries · organic cathode · porphyrin · electrochemical performance

- [1] J. M. Tarascon, M. Armand, *Nature* **2001**, *414*, 359–367.
- [2] J. W. Choi, D. Aurbach, *Nat. Rev. Mater.* **2016**, *1*, 16013.
- [3] T. Leisegang, F. Meutzner, M. Zschornak, W. Münchgesang, R. Schmid, T. Nestler, R. A. Eremin, A. A. Kabanov, V. A. Blatov, D. C. Meyer, *Frontiers in chemistry* **2019**, *7*.
- [4] a) N. Zhu, K. Zhang, F. Wu, Y. Bai, C. Wu, *Energy Material Advances* **2021**, *2021*, 9204217; b) J. Tu, W.-L. Song, H. Lei, Z. Yu, L.-L. Chen, M. Wang, S. Jiao, *Chem. Rev.* **2021**, *121*, 4903–4961.
- [5] a) Z. Huang, X. Du, M. Ma, S. Wang, Y. Xie, Y. Meng, W. You, L. Xiong, *ChemSusChem* **2023**, *16*, e202202358; b) Z. Yang, F. Wang, P. Meng, J. Luo, C. Fu, *Energy Storage Mater.* **2022**, *51*, 63–79.
- [6] M.-C. Lin, M. Gong, B. Lu, Y. Wu, D.-Y. Wang, M. Guan, M. Angell, C. Chen, J. Yang, B.-J. Hwang, H. Dai, *Nature* **2015**, *520*, 324–328.
- [7] a) H. Lu, Y. Wan, T. Wang, R. Jin, P. Ding, R. Wang, Y. Wang, C. Teng, L. Li, X. Wang, D. Zhou, G. Xue, *J. Mater. Chem. A* **2019**, *7*, 7213–7220; b) J. Tu, M. Wang, Y. Luo, S. Jiao, *ACS Sustainable Chem. Eng.* **2020**, *8*, 2416–2422.
- [8] a) Z. Zhao, Z. Hu, Q. Li, H. Li, X. Zhang, Y. Zhuang, F. Wang, G. Yu, *Nano Today* **2020**, *32*, 100870; b) K. Liang, L. Ju, S. Koul, A. Kushima, Y. Yang, *Adv. Energy Mater.* **2019**, *9*, 1802543; c) L. Fang, L. Zhou, L. Cui, P. Jiao, Q. An, K. Zhang, *J. Energy Chem.* **2021**, *63*, 320–327.
- [9] a) Y. Ai, S.-C. Wu, K. Wang, T.-Y. Yang, M. Liu, H.-J. Liao, J. Sun, J.-H. Chen, S.-Y. Tang, D. C. Wu, T.-Y. Su, Y.-C. Wang, H.-C. Chen, S. Zhang, W.-W. Liu, Y.-Z. Chen, L. Lee, J.-H. He, Z. M. Wang, Y.-L. Chueh, *ACS Nano* **2020**, *14*, 8539–8550; b) L. Yao, S. Ju, T. Xu, X. Yu, *ACS Nano* **2021**, *15*, 13662–13673.
- [10] H. Li, R. Meng, Y. Guo, B. Chen, Y. Jiao, C. Ye, Y. Long, A. Tadich, Q.-H. Yang, M. Jaroniec, S.-Z. Qiao, *Nat. Commun.* **2021**, *12*, 5714.
- [11] a) J. Bitenc, N. Lindahl, A. Vizintin, M. E. Abdelhamid, R. Dominko, P. Johansson, *Energy Storage Mater.* **2020**, *24*, 379–383; b) X. Fan, F. Wang, X. Ji, R. Wang, T. Gao, S. Hou, J. Chen, T. Deng, X. Li, L. Chen, C. Luo, L. Wang, C. Wang, *Angew. Chem. Int. Ed.* **2018**, *57*, 7146–7150; c) J. Zhou, X. Yu, J. Zhou, B. Lu, *Energy Storage Mater.* **2020**, *31*, 58–63; d) S. Wang, S. Huang, M. Yao, Y. Zhang, Z. Niu, *Angew. Chem. Int. Ed.* **2020**, *59*, 11800–11807; e) T. Sun, Q.-Q. Sun, Y. Yu, X.-B. Zhang, *eScience* **2021**, *1*, 186–193.
- [12] D. J. Kim, D.-J. Yoo, M. T. Otley, A. Prokofjevs, C. Pezzato, M. Owczarek, S. J. Lee, J. W. Choi, J. F. Stoddart, *Nat. Energy* **2019**, *4*, 51–59.
- [13] X. Han, S. Li, W.-L. Song, N. Chen, H. Chen, S. Huang, S. Jiao, *Adv. Energy Mater.* **2021**, *11*, 2101446.
- [14] M. Ballester, L. Ravotto, J. M. E. Quirke, R. López de la Vega, J. A. Shelnutt, A. V. Cheprakov, S. A. Vinogradov, C. J. Medforth, *J. Phys. Chem. A* **2020**, *124*, 8994–9003.
- [15] a) E. Abouzari-Lotf, R. Azmi, Z. Li, S. Shakouri, Z. Chen, Z. Zhao-Karger, S. Klyatskaya, J. Maibach, M. Ruben, M. Fichtner, *ChemSusChem* **2021**, *14*, 1840–1846; b) Z. Chen, P. Gao, W. Wang, S. Klyatskaya, Z. Zhao-Karger, D. Wang, C. Kübel, O. Fuhr, M. Fichtner, M. Ruben, *ChemSusChem* **2019**, *12*, 3737–3741; c) Z. Zhao-Karger, P. Gao, T. Ebert, S. Klyatskaya, Z. Chen, M. Ruben, M. Fichtner, *Adv. Mater.* **2019**, *31*, 1806599; d) S. Lv, J. Yuan, Z. Chen, P. Gao, H. Shu, X. Yang, E. Liu, S. Tan, M. Ruben, Z. Zhao-Karger, M. Fichtner, *ChemSusChem* **2020**, *13*, 2286–2294.
- [16] M.-S. Liao, S. Scheiner, *J. Chem. Phys.* **2002**, *117*, 205–219.
- [17] G. Wang, E. Dmitrieva, B. Kohn, U. Scheler, Y. Liu, V. Tkachova, L. Yang, Y. Fu, J. Ma, P. Zhang, F. Wang, J. Ge, X. Feng, *Angew. Chem. Int. Ed.* **2022**, *61*, e202116194.
- [18] S. Shakouri, E. Abouzari-Lotf, J. Chen, T. Diemant, S. Klyatskaya, F. D. Pammer, A. Mizuno, M. Fichtner, M. Ruben, *ChemSusChem* **2023**, *16*, e202202090.
- [19] J. Liu, X. Yang, L. Sun, *Chem. Commun.* **2013**, *49*, 11785–11787.
- [20] G. Studer, A. Schmidt, J. Büttner, M. Schmidt, A. Fischer, I. Krossing, B. Esser, *Energy Environ. Sci.* **2023**, *16*, 3760–3769.
- [21] a) J.-Y. Shin, T. Yamada, H. Yoshikawa, K. Awaga, H. Shinokubo, *Angew. Chem. Int. Ed.* **2014**, *53*, 3096–3101; b) P. Gao, Z. Chen, Z. Zhao-Karger, J. E. Mueller, C. Jung, S. Klyatskaya, T. Diemant, O. Fuhr, T. Jacob, R. J.

- Behm, M. Ruben, M. Fichtner, *Angew. Chem. Int. Ed.* **2017**, *56*, 10341–10346.
- [22] a) J. Wang, H. Liu, C. Du, Y. Liu, B. Liu, H. Guan, S. Guan, Z. Sun, H. Yao, *Chem. Sci.* **2022**, *13*, 11614–11622; b) M. Charlton, T. D. Hatchard, M. N. Obrovac, *J. Electrochem. Soc.* **2020**, *167*, 080501.
- [23] a) F. Otteny, V. Perner, D. Wassy, M. Kolek, P. Bieker, M. Winter, B. Esser, *ACS Sustainable Chem. Eng.* **2020**, *8*, 238–247; b) J. Yuan, B. Ren, X. Feng, P. Gao, E. Liu, S. Tan, *Chem. Commun.* **2020**, *56*, 5437–5440; c) L. Gong, X. Yang, Y. Gao, G. Yang, Z. Yu, X. Fu, Y. Wang, D. Qi, Y. Bian, K. Wang, J. Jiang, *J. Mater. Chem. A* **2022**, *10*, 16595–16601.
- [24] A. Riaz, M. R. Sarker, M. H. Saad, R. Mohamed, in *Sensors*, Vol. 21, 2021.
- [25] V. Augustyn, J. Come, M. A. Lowe, J. W. Kim, P.-L. Taberna, S. H. Tolbert, H. D. Abruña, P. Simon, B. Dunn, *Nat. Mater.* **2013**, *12*, 518–522.
- [26] J. M. Campiña, *J. Electrochem. Soc.* **2015**, *162*, H142.
- [27] N. J. Stone, *At. Data Nucl. Data Tables* **2005**, *90*, 75–176.
- [28] K. Susumu, P. R. Frail, P. J. Angiolillo, M. J. Therien, *J. Am. Chem. Soc.* **2006**, *128*, 8380–8381.
- [29] a) Q. Huang, J. Chen, X. Shao, L. Zhang, Y. Dong, W. Li, C. Zhang, Y. Ma, *Chem. Eng. J.* **2023**, *461*, 141974; b) S. Chen, T. Jia, G. Zhou, C. Zhang, Q. Hou, Y. Wang, S. Luo, G. Shi, Y. Zeng, *J. Electrochem. Soc.* **2019**, *166*, A2543.
- [30] J. R. Weinkauf, S. W. Cooper, A. Schweiger, C. C. Wamser, *J. Phys. Chem. A* **2003**, *107*, 3486–3496.
- [31] a) C. Wang, C. C. Wamser, *J. Org. Chem.* **2015**, *80*, 7351–7359; b) A. B. Rudine, B. D. DelFatti, C. C. Wamser, *J. Org. Chem.* **2013**, *78*, 6040–6049.
- [32] Z. Li, B. Niu, Y. Liu, J. Li, F. Kang, *Electrochim. Acta* **2018**, *263*, 68–75.

Manuscript received: December 9, 2023

Revised manuscript received: January 17, 2024

Accepted manuscript online: January 19, 2024

Version of record online: January 29, 2024